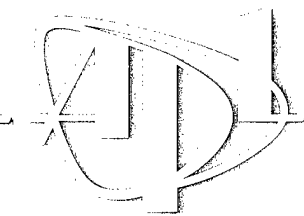


Nonlinear Wave Propagation with Implications for Mine Neutralization

by Steven G. Kargl

19981027015

Technical Report
APL-UW TR 9803
September 1998



Applied Physics Laboratory University of Washington
Seattle, Washington 98105-6698

Contract N00039-91-C-0072

ACKNOWLEDGMENTS

This report was sponsored by the Office of Naval Research, Code 321, Tactical Sensing, with technical management by Randall Jacobson. Funding was provided through contract N00039-91-C-0072 (Task Description 03C2044) entitled "Remote Acoustical Mine Neutralization Using Back-Propagated Shock Waves."

ABSTRACT

Prototype devices that use pulse-power techniques to generate an intense acoustical field in water have fostered a renewed interest in applying finite-amplitude sound to the mine-neutralization problem, particularly in a littoral region. A simple intuitive description of acoustical mine neutralization includes three basic processes: (1) generation of the acoustical field at the source; (2) nonlinear wave propagation; and (3) neutralization mechanisms at the target. This document focuses on the second issue, the propagation of an intense acoustical field from a source to a target. The research discussed here provides a theoretical foundation for a modeling effort, describes several case studies, and gives empirical rules for establishing the material parameters of fresh and sea water required by the theory. Several key issues are presented, including the breakdown of using linear superposition of the results for discrete sources in an array, phasing an array of discrete sources for beam steering, and peak positive and negative pressures.

CONTENTS

1. INTRODUCTION	1
2. CASE STUDIES	5
2.1 Boston University Experiments	5
2.2 Fresh Water Lake	11
3. THEORETICAL DEVELOPMENT	15
3.1 Augmented Khokhlov-Zabolotskaya-Kuznetsov Equation	15
3.2 Axisymmetric Circular Source	15
3.3 Rectangular Source	18
4. NUMERICAL SOLUTION	19
4.1 Diffraction Algorithm	20
4.2 Thermoviscous Absorption Algorithm	21
4.3 Quadratic Nonlinearity Algorithm	22
4.4 Relaxation Algorithm	23
APPENDIX, Empirical Material Parameters for Water	24
REFERENCES	28

LIST OF FIGURES

Figure 1.	Retarded time traces along the acoustic axis at 25 kPa	7
Figure 2.	Retarded time traces along the acoustic axis at 125 kPa	7
Figure 3.	Retarded time traces along the acoustic axis at 225 kPa	8
Figure 4.	Retarded time traces along the acoustic axis at 325 kPa	8
Figure 5.	Center two cycles from Figures 1(e)–4(e)	9
Figure 6.	Time-averaged energy flux along acoustics axis	10
Figure 7.	Retarded time traces produced by a phased array in a fresh water lake	13
Figure 8.	Retarded time traces for a phased array and focused piston transducer	13
Figure 9.	Time-averaged energy flux for an array in a fresh water lake	14
Figure 10.	Graphical depiction of the nonlinear distortion algorithm	22

1. INTRODUCTION

Before intense acoustic fields can be employed as a means of neutralizing mines remotely, several critical issues regarding nonlinear wave propagation need to be addressed and clarified. When a finite-amplitude wave propagates in a fluid, four basic physical phenomena affect the wave propagation. These phenomena are nonlinearity, thermoviscous absorption, relaxation, and diffraction. A brief description of each is given below. Other critical issues for the neutralization of mines with finite-amplitude waves include environmental conditions, beam forming (phasing an array of discrete sources), expected peak pressure amplitude (acoustic saturation), and signal duration. To date, no comprehensive study has considered these issues as they relate to nonlinear wave propagation in an ocean environment and a mine countermeasure (MCM) scenario.

Nonlinearity has important implications for finite-amplitude waves. Nonlinearity causes steepening of the pulse, which ultimately leads to shock formation. The propagation velocity of the finite-amplitude wave depends on the local sound pressure. A higher positive pressure produces a higher speed. Thus, a wave crest moves faster than a trough, causing the wave to steepen. As a consequence, energy from lower-frequency components is repartitioned to higher-frequency components. Thus nonlinearity is not a direct mechanism of energy loss; however, the pumping of energy to higher frequencies leads to energy loss through thermoviscous absorption and relaxation processes.

Energy loss through thermoviscous absorption results in a heating of the fluid. A finite-amplitude wave imparts some momentum to a “parcel” of fluid. As adjacent parcels of fluid “rub” against one another, energy is converted to heat through frictional forces. This mechanism is directly related to the thermal and viscous properties of the fluid through the attenuation coefficient. This coefficient is frequency dependent such that higher-frequency components of a pulse will be more strongly attenuated than lower-frequency components. For fresh and sea water, the thermoviscous attenuation coefficient goes as f^2 , where f denotes frequency.

Although relaxation is an energy loss mechanism, it differs from thermoviscous absorption because it depends on the presence of impurities. In the ocean, the two primary sources of relaxation are magnesium sulfate [1], $MgSO_4$, and boric acid [2], H_3BO_3 , which dissipate energy through chemical activity (e.g., chemical dissociation or increased vibrational or rotational energy of a molecule). In addition, relaxation processes give rise to dispersion (frequency-dependent phase velocity) which leads to temporal spreading of the pulse. Higher-frequency components of a pulse typically propagate with a faster phase velocity, stretching the pulse.

Diffraction is associated with the finite aperture of a directive source. Its main contribution to the wave propagation problem is a spatial spreading of the energy. Although geometric focusing, beam forming, and amplitude shading can reduce the spreading for a bounded beam source, diffraction eventually sets in beyond the focal zone.

The environment has severe implications for finite-amplitude-wave neutralization of mines. Bubbles are present in sufficient quantity in shallow and very shallow water such that even linear acoustics is altered [3, 4]. These bubbles may be entrained from breaking waves in the surf zone or advected from deeper water by currents. Bubbles can be stabilized by a thin coating of surfactant, and the lifetime of such a bubble can greatly exceed the lifetime of a similar, clean bubble in fresh water. With respect to nonlinear wave propagation, bubbles cause a significant increase in β , the coefficient of nonlinearity. For fresh and sea water without bubbles, β is nominally 3.5 and 3.6, respectfully. The addition of even a small number density and bubble size distribution can increase β by several orders of magnitude, with values reported as large as 31,000 [5]. With this increase in nonlinearity, one might assume that finite-amplitude wave propagation will become “easier”; however, the bubbles affect the dispersion and attenuation of sound in water as well. Thus, the presence of bubbles complicates the analysis such that they cannot be ignored.

Bubbles in the presence of an intense acoustic field provide sites for cavitation. For a transient-type shock pulse, a region of negative pressure (relative to the ambient hydrostatic value) follows the large compressional shock. During this negative pressure, any bubbles present will experience rapid growth from their initial equilibrium size. After the negative pressure passes, the bubbles will collapse, with subsequent acoustic radiation. This radiation may be beneficial or detrimental to MCM, but proper analyses is beyond the scope of this document.

Nonlinear wave propagation in shallow and very shallow water necessarily implies that one must consider the air-sea and sea-sediment boundaries. For a transient excitation, ray tracing provides sufficient information to determine if multipaths will (or will not) affect the direct arrival at a target. For example, if a source and target are 5 m below the air-sea interface and separated by 100 m, then the first surface bounce will have a 0.5 m longer pathlength than the direct ray in a homogeneous ocean. This implies that the surface bounce will arrive at the target approximately 0.3 ms after the direct pulse. If the pulse duration exceeds 0.3 ms, then the direct arrival and the multipath arrival will interfere. Furthermore, the reflection of a pressure pulse from the air-sea interface will invert the phase of the pulse. Water cannot sustain a large negative pressure (relative to the hydrostatic pressure) without cavitation. Hence, the negative portion of a pressure pulse may cause a local increase in the bubble number density, leading to additional dissipation near the interface.

When linear acoustics applies, beam forming is a well-known method for focusing and directing acoustic energy. With properly designed sources, the air-sea and sea-sediment boundaries are no longer an issue. Unfortunately, when the source levels of individual elements of an array are sufficient for nonlinearity to become an issue, the degree to which beam forming can be achieved is unknown. Only a limited investigation has been conducted of the nonlinear behavior of two discrete point sources in the quasilinear approximation [6, 7, 8]. A generalization of that analysis to an array of point sources appears possible; however, an array of discrete spark-gap sources, though point-like, will produce source levels that invalidate some assumptions required by the quasilinear approximation. Applying ordinary linear acoustics with absorption, relaxation, and diffraction to a finite-amplitude wave propagation problem will lead to an erroneous result. Proper inclusion of nonlinearity is essential to correctly model nonlinear wave propagation from a distribution of discrete, intensive, sound sources. This claim will be substantiated in the following discussion.

At the higher source levels expected of pulse-power discrete arrays, beam forming may become more difficult. Consider a two-source array where the field from source 1 is time delayed relative to that from source 2, and the fields from 1 and 2 are sufficient for shock formation. The Rankine-Hugoniot conditions for source 1 suggest that its shock front will propagate with a higher velocity than the shock front from source 2. This implies that the shock front from source 1 may overtake the shock front from source 2 prior to their arrival at a target unless the initial delay properly accounts for the higher propagation speed of the shock front from source 1. The subsequent interaction of the fields from sources 1 and 2 may not produce the desired effect at the target.

The peak pressure achievable from conventional source technology appears to be limited to less than 200 MPa except for explosive sources (higher peak pressures may be achieved from focusing). This suggests nonlinear acoustics, where cubic and higher-order terms in the standard acoustic field variables are neglected, can be used to analyze the field produced by these sources. Nonlinear acoustics applies when the acoustic Mach number satisfies $\epsilon \equiv p_0/\rho_0 c_0^2 \ll 1$, where p_0 , ρ_0 , and c_0 are the peak positive pressure, the ambient density of the fluid, and the small-signal sound speed, respectively. The definition of the Mach number given here assumes that the energy is propagating primarily in one direction and a progressive plane wave approximation of $p_0 = \rho_0 c_0 u_0$ holds, where u_0 is a typical acoustic particle velocity. Hence, a peak pressure of 200 MPa gives $\epsilon = p_0/\rho_0 c_0^2 \approx 0.1$, and the theoretical treatment discussed here can be used. However, if the peak pressure is expected to exceed 200 MPa, then nonlinear acoustics may not yield reliable results. The only recourse is a numerical solution based on the fundamental equations of fluid dynamics (conservation of mass, momentum, and energy, and an appropriate equation of state for the fluid).

Initial computations for the nonlinear wave propagation can be based on either the Khokhlov-Zabolotskaya-Kuznetsov (KZK) equation or the nonlinear progressive wave equation (NPE). Both the KZK and NPE are parabolic wave equations which are valid within a small angle along the axis of propagation. Methods for the numerical computation of the KZK or NPE model are easily found in the recent acoustics literature [9, 10, 11, 12]. An augmented KZK equation explicitly includes quadratic nonlinearity, thermoviscous absorption, relaxation, and diffraction, which permits independent investigation of each physical mechanism. This document concentrates on theoretical results produced by a numerical implementation of an augmented KZK equation [13].

Acoustic saturation is normally associated with continuous wave (CW) radiation from a source at a fundamental frequency with sufficient intensity to cause nonlinear processes to be important [14, 15]. However, acoustic saturation may affect a field from a source with a finite, but long, pulse with a fundamental frequency (e.g., a tone burst from a magnetostrictive piston source). A simple explanation of acoustic saturation is that energy in the fundamental frequency is pumped into higher harmonics. That is, once the fundamental frequency component has reached saturation, any further attempt to increase the energy in the fundamental frequency dumps energy into the higher harmonics. Thus, the pulse undergoes nonlinear distortion, leading to shock formation. Acoustic saturation may not be an important effect for the transient fields expected from pulse-power systems because quadratic nonlinearity is a cumulative effect.

2. CASE STUDIES

2.1 Boston University Experiments

The first case study considers conditions that are well suited to test the robustness of the theory and numerical algorithms discussed in greater detail in Sections 3 and 4. Edson and Roy at Boston University (BU) conducted several experiments involving nonlinear wave propagation from an eight-element annular array [16]. Equipment failure in the generation of eight independent source waves prevented the use of the outermost annular element of the array, and thus the simulations discussed here are limited to a seven-element annular array.

The BU experiments were conducted in filtered, deionized water. The dissolved gas content of the water was reduced to 85% of saturation to inhibit cavitation. The ambient pressure was approximately 1 atm, and the salinity of the water throughout the experiments was 0 ppt (i.e., fresh water). Attempts to maintain a constant ambient temperature were not implemented. Each experiment started with an ambient temperature dictated by the room temperature of the laboratory (nominally, 17°C). Edson and Roy reported an upward drift of the temperature of no more than 5°C over the duration of an experiment. They attributed the drift to the proximity of the water tank to the seven power amplifiers used to drive the individual elements of the array. For the computations included here, the ambient pressure, temperature, and salinity are set to 1 atm, 17°C, and 0 ppt. All required material parameters for the water are then computed via the empirical rules in the appendix.

The array consisted of a center circular element and six concentric rings. Each element was constructed from a 1-3 piezocomposite, the center frequency of the array was 480 kHz, and the bandwidth was 210 kHz. The surface area of an element was 18.85 cm², and the radius of the innermost element was 2.45 cm. In the progressive wave approximation for a given source amplitude, the energy flux from any one element is equivalent to that from any of the others. A 0.03-cm gap separated adjacent elements, which were coplanar. The elements (and auxiliary electronics) were independent and isolated to reduce cross-talk and permit phasing of the array to adjust the depth of focus.

The source waveform reported by Edson and Roy was a 10-cycle sine wave tone burst with temporal shading. No amplitude shading across the array was used in the experiments. The pressure in the source plane for the n th element was

$$p_n(R, \sigma = 0, \tau) = p_0 \exp\{-(\tau + \psi_n)/N\pi\} \sin(\tau + \psi_n), \quad (1)$$

where ψ_n is a phase relative to that of the center element and is adjusted to focus the array at 24 cm from the face of the array. Equation (1) is expressed in a form

such that R and σ are dimensionless radial and z coordinates and τ is a dimensionless retarded time. The coefficient m controls the rise time of the temporal envelope and N is the number of cycles, which governs the total length of the pulse. When $m = 1$, the envelope defined by the exponential factor in (1) becomes the familiar Gaussian envelope. A sequence of experiments was performed in which p_0 was set to 20, 44, 200, 300, 400, and 465 kPa. For the computations reported here, the pulse contains five cycles and p_0 has been set to 25, 125, 225, and 325 kPa. These choices were dictated by limitations on the available computational facilities (see Section 4 for further comments).

In the computations, the phase of each element must be set to an appropriate value relative to the phase of the center element to cause the desired focusing. This is accomplished by setting $\psi_0 = 0$ and $\psi_n = G\bar{R}_n$ ($n > 0$), where G is the focusing gain (proportional to the ratio of the outer radius of the array to the focal length) and \bar{R} is the mean radius of an element. The choice of \bar{R} is somewhat arbitrary; it could have been set, for example, to either the inner or outer radius of each ring.

Figures 1–4 correspond to retarded time traces at various locations, σ , along the acoustic axis of the array for source amplitudes of 25, 125, 225, and 325 kPa, respectively. These locations are (a) 0.2, (b) 0.4, (c) 0.6, (d) 0.8, (e) 1.0, and (f) 1.2 where the normalization is the focal length of 24 cm. Although not apparent in all the figures, panels (a)–(d) and (f) contain two curves, a solid curve showing the results when all array elements are driven simultaneously with the proper phase, and a long dashed curve showing a linear superposition of the possibly nonlinear acoustic field when each element is driven independently (but with the proper phase). Panel (e) in each figure is similar to the other panels except a third curve is included: a short dashed curve that shows the time trace produced by a single continuous element that is spherically focused at 24 cm (i.e., a focused circular piston transducer). The significance of this curve is that it is the upper limit on the expected field when the number of array elements becomes large. Finally, as a side note, the shape of the pulse in Figure 1(d) is essentially the shape of the pulse in the initial source plane as given by (1).

Clearly, Figure 1 demonstrates that at a low source amplitude linear superposition may be applied to the acoustic fields produced by an array of discrete sources. This permits a substantial reduction in the computational complexity and allows more general array geometries. As the source amplitude is increased, however, the effects of nonlinearity become important, particularly in the vicinity of the focus. To illustrate this point, the center two cycles of Figures 1(e), 2(e), 3(e), and 4(e) are reproduced in Figure 5 without the additional third curve. To reiterate, the solid curve represents the acoustic field when all elements are operated simultaneously, and the dashed curve depicts the linear superposition of the fields from the individual elements when nonlinear wave propagation is permitted for those fields.

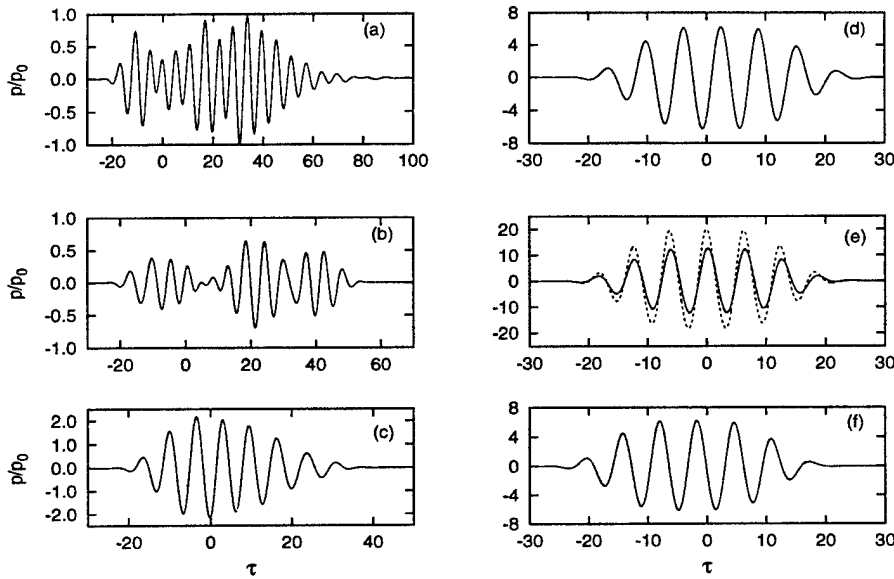


Figure 1. Retarded time traces along the acoustic axis of a seven-element annular array at the following σ locations: (a) 0.2, (b) 0.4, (c) 0.6, (d) 0.8, (e) 1.0, and (f) 1.2. The pressure amplitude in the source plane is $p_0 = 25$ kPa.

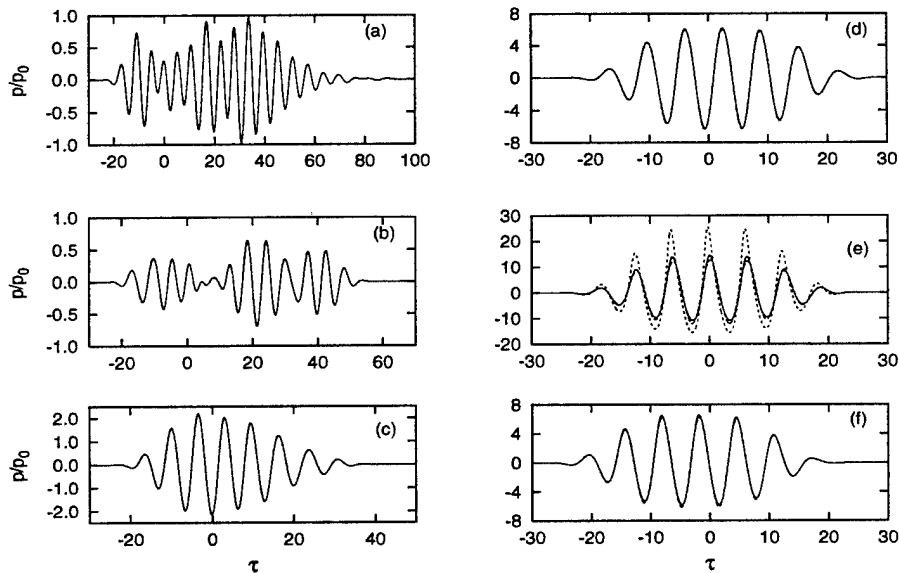


Figure 2. Retarded time traces along the acoustic axis of a seven-element annular array at the following σ locations: (a) 0.2, (b) 0.4, (c) 0.6, (d) 0.8, (e) 1.0, and (f) 1.2. The pressure amplitude in the source plane is $p_0 = 125$ kPa.

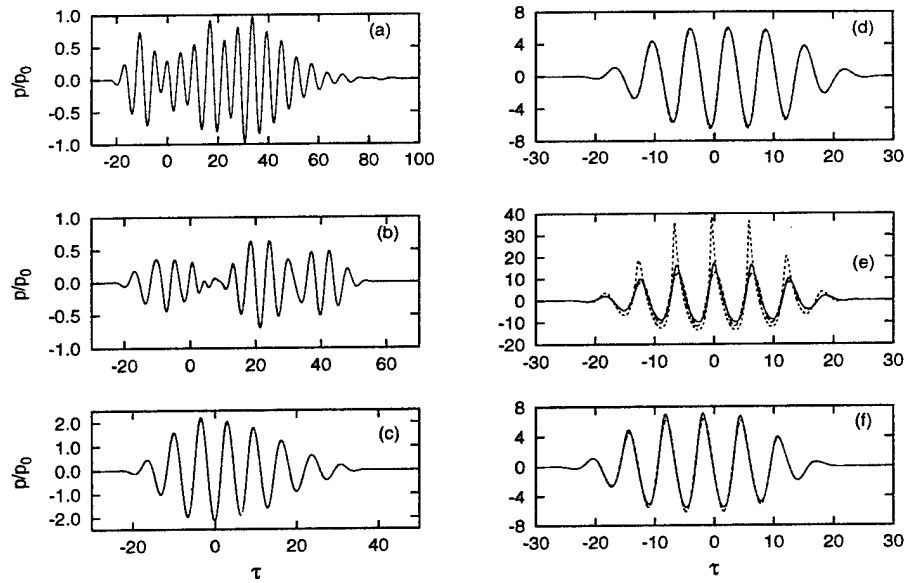


Figure 3. Retarded time traces along the acoustic axis of a seven-element annular array at the following σ locations: (a) 0.2, (b) 0.4, (c) 0.6, (d) 0.8, (e) 1.0, and (f) 1.2. The pressure amplitude in the source plane is $p_0 = 225$ kPa.

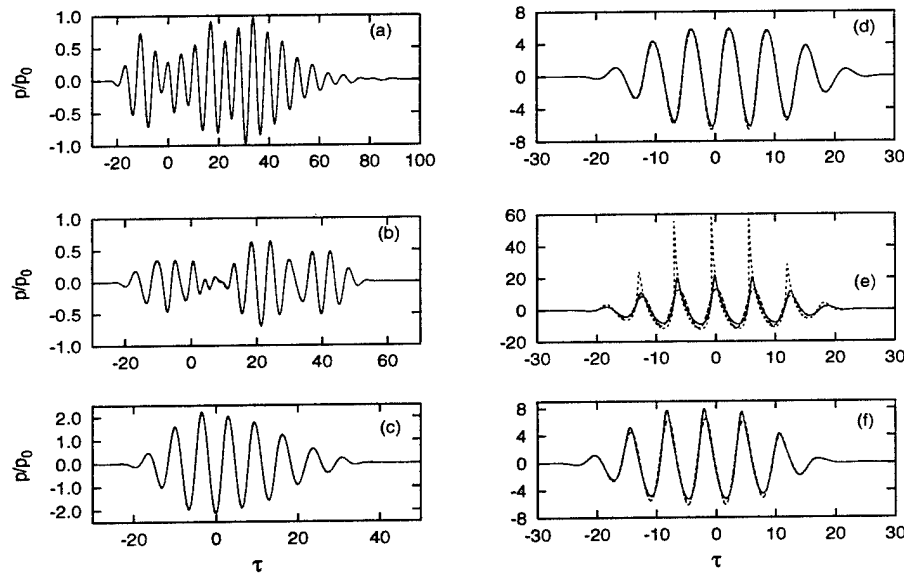


Figure 4. Retarded time traces along the acoustic axis of a seven-element annular array at the following σ locations: (a) 0.2, (b) 0.4, (c) 0.6, (d) 0.8, (e) 1.0, and (f) 1.2. The pressure amplitude in the source plane is $p_0 = 325$ kPa.

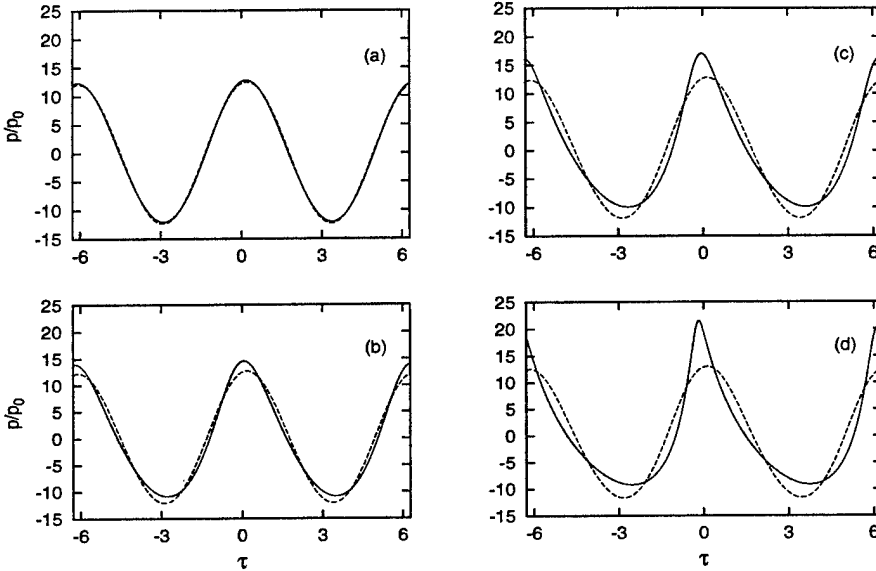


Figure 5. The center two cycles from (a) Figure 1(e), (b) Figure 2(e), (c) Figure 3(e), and (d) Figure 4(e). The solid curve is the results when driving the array elements simultaneously (with the proper phase). The dashed curve corresponds to a linear superposition of the acoustic fields from the individual elements.

Inspection of Figure 5 shows that three important features occur as the source amplitude is increased. First, the expected peak positive pressure, P_+ , is underpredicted by linear superposition of the independent nonlinear fields. At the highest source level, P_+ from a properly phased array is approximately 65% greater than the simple linear superposition predicts. The second feature involves the peak negative pressure, P_- . Linear superposition overpredicts P_- although the severity of the error is only about 20%. The importance of P_+ and P_- with respect to mine neutralization has not been established. The third and final feature is the shape of the two waveforms in each panel of Figure 5. It is well known that nonlinear wave propagation shifts energy from the fundamental frequency, 500 kHz for this case study, to higher harmonics. The degree of waveform distortion is directly related to the content of the higher harmonics produced such that a more distorted pulse contains more harmonics. When the acoustic fields are propagated independently and then linearly summed, the shifting of energy to higher harmonics is artificially quenched.

Although the source amplitudes used to produce Figure 1–5 differ from those reported by Edson and Roy, these computations support their conclusions because their source levels of 20, 100, 200, and 300 kPa are close to those used here. In fact, Figures 1(e) and 3(e) agree fairly well with Figures 5 and 7 given by Edson and Roy for their 20 and 200 kPa experiments [16].

Figures 1 through 4 provide information at selected locations along the acoustical axis of the array. These locations may not provide the *best choice* with respect to local maxima in P_+ and $|P_-|$. Treating P_+ and $|P_-|$ as a function of σ is appealing; however, as Figure 1(b) suggests, complicated constructive and destructive interference may obfuscate these waveform features. Thus, a time-average energy flux density in the direction of propagation seems to provide a good measure. The energy flux vector is defined as $\vec{j} = p\vec{u}$, and within the progressive wave approximation this reduces to $j_z = p_0^2 P^2 / \rho_0 c_0$, where here p_0 is the source amplitude and P is a normalized pressure. The time average is computed across the entire retarded time window,

$$\langle j_z \rangle = \frac{p_0^2}{\rho_0 c_0 (\tau_M - \tau_m)} \int_{\tau_m}^{\tau_M} P^2 d\tau', \quad (2)$$

such that τ_m and τ_M are the minimum and maximum of the time window. Figure 6 depicts $\langle j_z \rangle$ for the seven element annular array (dashed curve) and a spherically focused piston transducer (solid curve). As a reminder, the outer radius of the piston source and the array are equivalent, and the relatively small separation between adjacent elements means the piston transducer and array deposit the same amount of energy into the total acoustic field.

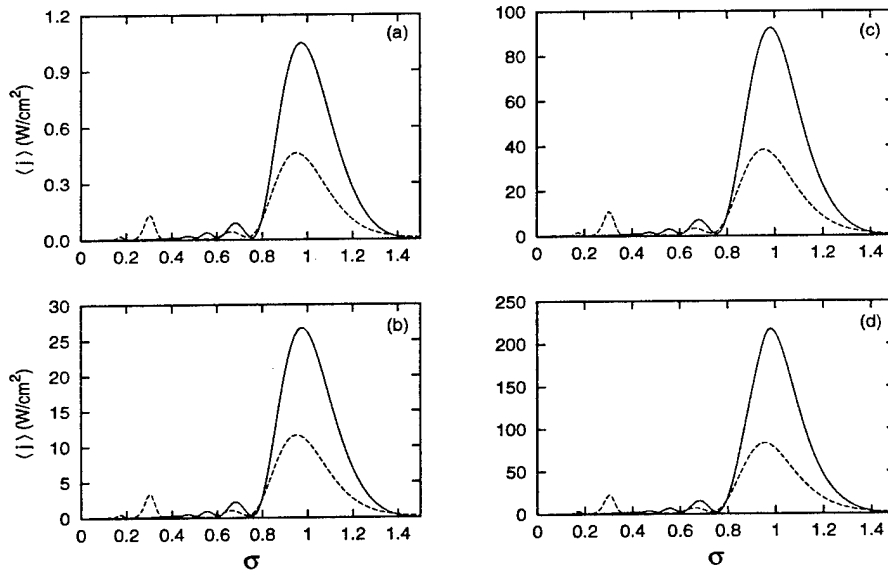


Figure 6. The time-averaged energy flux along the acoustic axis of the transducer. (a) $p_0 = 25$ kPa; (b) $p_0 = 125$ kPa; (c) $p_0 = 225$ kPa; and (d) $p_0 = 325$ kPa. The solid curve shows the results for a spherically focused piston transducer and the dashed curve shows the results for a phased array.

Two important features are immediately evident in Figure 6. First, the curve for the array contains a strong peak near $\sigma = 0.3$. The peak is due to a combination of the small number of elements and their finite dimensions. The ratio of this peak's value to the peak value at the focus appears to be weakly dependent on p_0 . This suggests that a prefocal "hot spot" may be a feature of an annular array source; its magnitude is expected to diminish with an increasing number of elements. The second, and perhaps most important, feature is the significant difference between a focused piston transducer and a phased array at all source amplitudes. This difference is due to the finite dimensions of the individual array elements. With a phase of $\psi_n = G\bar{R}_n$, it is clear that the energy allotted to the portion of the element with $R < \bar{R}_n$ has already arrived at and passed through the focus, while the energy allotted to the portion of the array element with $R > \bar{R}_n$ has not reached the focus. As the number of array elements is increased, the surface area of each element is reduced, and the phased array result approaches the upper limit for a spherically focused piston transducer. Hence, any simulation of an array of intense sources must be carefully performed.

It is noteworthy to briefly discuss the peak values of P_+ and $|P_-|$ although figures for this case study will not be presented. At a source amplitude of $p_0 = 25$ kPa, the acoustic fields from the focused piston transducer and the array attain their largest values at a prefocal distance. That is, the geometric focus is at $\sigma = 1$, but the peak values occur slightly before $\sigma = 1$. As the source amplitude is increased, the peak values shift through the geometric focus and subsequently occur at $\sigma > 1$. Averkiou and Hamilton discuss a shift of peak values from the geometric focus when P_+ and $|P_-|$ are measured along the axis of a focused circular piston operating at 2.25 MHz [17].

2.2 Fresh Water Lake

The computations discussed above in Section 2.1 and their agreement with the results of the BU experiments suggest that the KZK formalism is well suited to analyzing nonlinear wave propagation from a phased array. However, all previous work, both computational and experimental, has considered frequencies and source dimensions that are inappropriate for MCM applications. This section discusses the predicted nonlinear behavior of a phased array in a fresh water lake.

The characteristics of the simulated phased array have been adjusted to a possible MCM system. The array contains 32 elements, and the surface area of each element is 0.0908 m^2 . The innermost element has an outer radius of 0.17 m, and the overall outer radius of the array is 1.004 m. The separation between adjacent elements is 0.002 m. The source condition is again given by (1), but the frequency has been

lowered to 100 kHz from the 500 kHz used in the BU experiments. The sine-wave tone burst contains five cycles. The source amplitude has also been lowered to 1, 10, 20, and 30 kPa. A mine countermeasure system requires a standoff distance of tens of meters. Hence, the geometric focus of the array has been set to 50 m.

The ambient water conditions have been adjusted to values that may occur in a fresh water littoral environment. The ambient pressure is 2 atm, which corresponds to an approximate depth of 10 m (i.e., the array is 10 m below the lake surface). The ambient temperature and salinity are 10°C and 0 ppt, respectively. Hence, relaxation processes are neglected in this simulation. Finally, the empirical rules for water are again used to determine the parameters required for the water.

Figures 7 and 8 compare retarded time traces at a dimensionless axial location of $\sigma = 0.8$, where the signals are near their maximum peak positive pressure. This corresponds to about 40 m from the array, and hence the peak response occurs at a prefocal region with respect to the geometric focus. Figure 7 demonstrates that linear superposition (dashed curve) of the fields from the array elements, when driven independently but with an appropriate phase delay, fails to reproduce the acoustic field from a properly phased array (solid curve) at high source amplitudes. The poor agreement shown in 7(b), 7(c), and 7(d) is due to the neglect of the nonlinear interaction between the fields from the individual elements. Figure 8 compares the field produced by the 32 element annular array (dashed curve) with that produced by a focused piston transducer (solid curve) with comparable source parameters. Within the resolution of Figure 8, these results are essentially indistinguishable. Hence, the claim in Section 2.1 that better agreement between an annular array and focused piston transducer will occur as the number of array elements increases is substantiated.

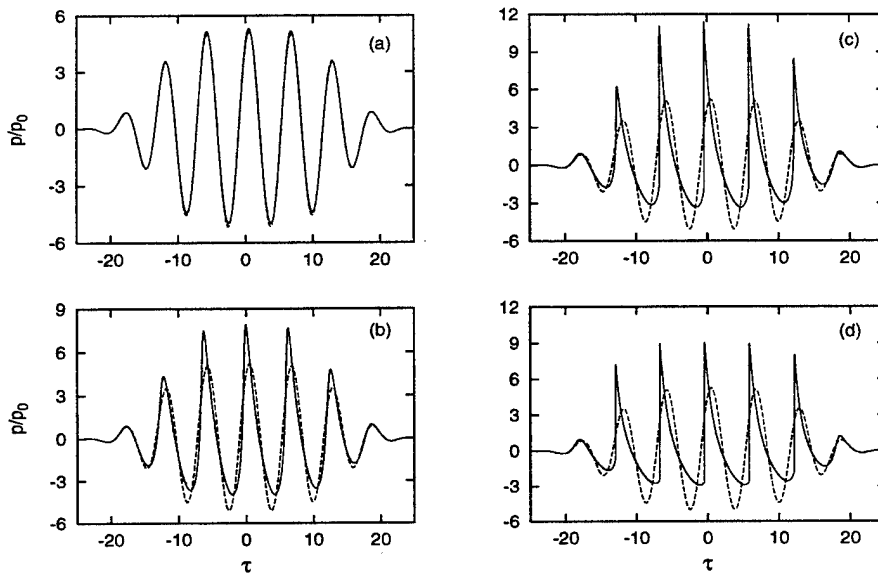


Figure 7. Linear superposition of the nonlinear fields from the independent array elements (dashed curve) and the acoustic field from a properly phased array (solid curve). (a) $p_0 = 1$ kPa, (b) $p_0 = 10$ kPa, (c) $p_0 = 20$ kPa, and (d) $p_0 = 30$ kPa. The dimensionless axial location is $\sigma = 0.8$.

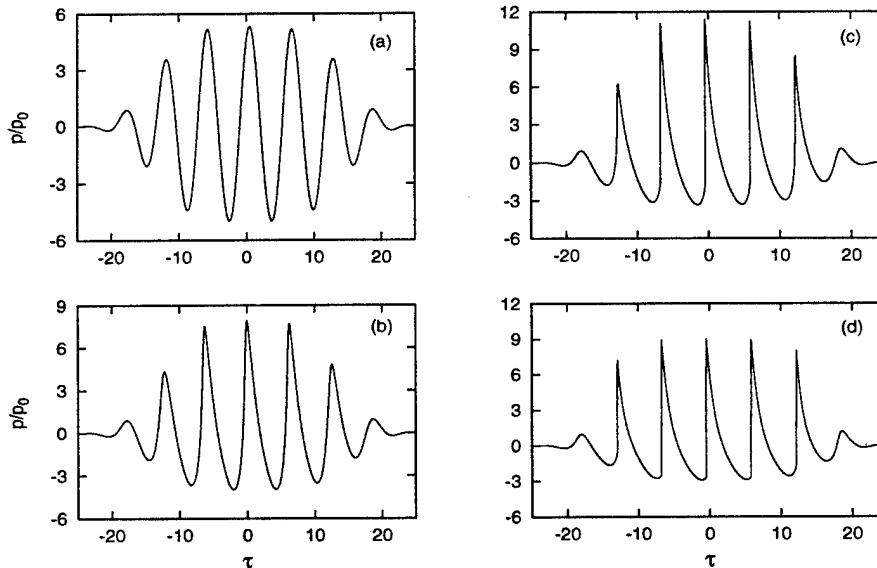


Figure 8. The acoustic fields from a properly phased array with 32 elements (dashed curve) and a focused piston source (solid curve). The sources produce similar results. The source amplitudes are (a) 1, (b) 10, (c) 20, and (d) 30 kPa. The dimensionless axial location is $\sigma = 0.8$.

A comparison of the time-averaged energy flux density, $\langle j_z \rangle$, is depicted in Figure 9. The dashed curve is the result obtained for the array, and the solid curve is the result produced by the focused piston source. Two features are immediately evident. First, the peak occurs near $\sigma = 0.7$ for $p_0 = 1, 10, \text{ and } 20 \text{ kPa}$, with a slight inward shift for $p_0 = 30 \text{ kPa}$. The prefocal maximum is similar to results reported by Hutchins et al. [18] for annular arrays and spherical bowl sources under linear acoustic conditions. However, the additional shift for $p_0 = 30 \text{ kPa}$ is due to the nonlinearity of the fluid. A second feature is the narrowing of the main peak at the higher source amplitudes of 20 and 30 kPa. This suggests the focal volume is slightly compressed at the higher source amplitudes, and the compression localizes the energy to a smaller volume about the focus. To fully quantify the acoustic field in the vicinity of the focus, $\langle j_z \rangle$ should be computed at off-axis locations along an axis transverse to the \hat{z} -direction. This procedure has not been implemented; however, the peak positive pressure as a function of the radial coordinate at the focus (i.e., the beam width) has been found to be in agreement with linear acoustics. Finally, under ordinary linear acoustics when the source amplitude is doubled (or tripled), then the resulting change in $\langle j_z \rangle$ is essentially a factor of 4 (or 9). Inspection of Figure 9 shows that a similar result does not hold. This behavior is due to the repartitioning of energy from the fundamental frequency to its higher harmonics and hence the subsequent higher energy loss from thermoviscous absorption.

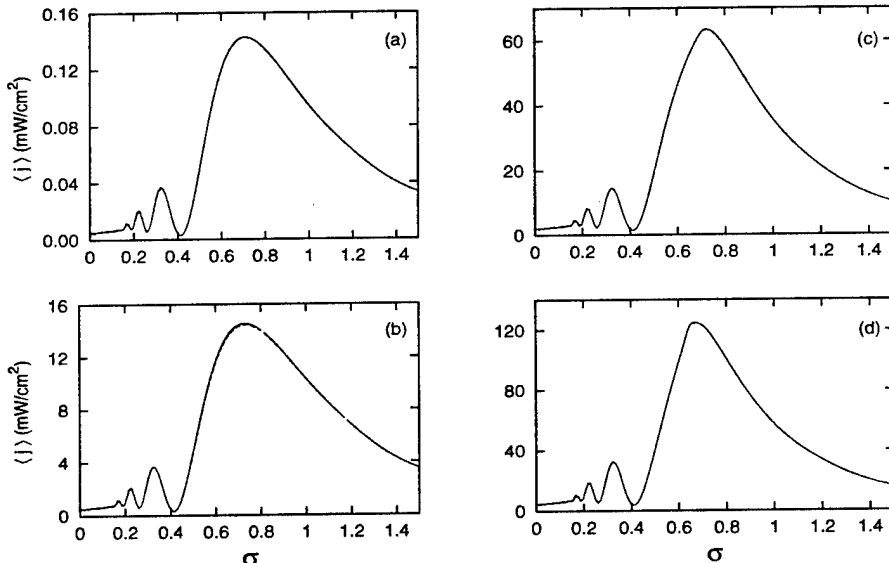


Figure 9. Comparison of the time-averaged energy flux density for a properly phased array with 32 elements (dashed curve) and a focused piston transducer (solid curve). The results agree. (a) $p_0 = 1 \text{ kPa}$, (b) $p_0 = 10 \text{ kPa}$, (c) $p_0 = 20 \text{ kPa}$, and (d) $p_0 = 30 \text{ kPa}$. The dimensionless axial location is $\sigma = 0.8$.

3. THEORETICAL DEVELOPMENT

3.1 Augmented Khokhlov-Zabolotskaya-Kuznetsov Equation

Cleveland et al. discuss a KZK nonlinear parabolic wave equation which has been augmented by including the relaxation processes within the fluid [13]. One form for the augmented KZK equation for pressure fluctuation, p , is

$$\frac{\partial^2 p}{\partial t' \partial z} = \frac{c_0}{2} \nabla_{\perp}^2 p + \frac{\delta}{2c_0^3} \frac{\partial^3 p}{\partial t'^3} + \frac{\beta}{2\rho_0 c_0^3} \frac{\partial^2 p^2}{\partial t'^2} + \sum_{\nu} \frac{1}{2\rho_0 c_0^3} \psi_{\nu} \frac{\partial^3 p}{\partial t'^3}, \quad (3)$$

where \perp denotes directions transverse to the propagation direction \hat{z} [19], $t' = t - z/c_0$ is a retarded time (that facilitates defining a temporal window which moves with a pulse), t is time, and δ is the diffusivity of sound; $\delta = [\zeta + 4\eta/3 + \kappa(c_v^{-1} - c_p^{-1})]/\rho_0$. The bulk and shear viscosity of the fluid are ζ and η , κ is the thermal conductivity, c_v is the specific heat at constant volume, and c_p is the specific heat at constant pressure. The relaxation operator for the ν th relaxation process is

$$\psi_{\nu} = \rho_0 c_0^2 \frac{m_{\nu} t_{\nu}}{1 + t_{\nu} \frac{\partial}{\partial t'}}; \quad (4)$$

t_{ν} is a relaxation time, and m_{ν} is a dimensionless quantity characterizing the dispersion of the relaxation process [20].

Although a progressive wave assumption, $p = \rho_0 c_0 u_z$, is required to arrive at (3), the first term on the right-hand side accounts for diffraction. That is, some energy propagates in the transverse direction, whereas it has been assumed that propagation primarily occurs along the \hat{z} axis. The second term accounts for thermoviscous absorption. It does not include relaxation processes, which are explicitly included by the last term. The third term represents quadratic nonlinearity. Harmonic generation, leading to shock formation, is accounted for by this term. Finally, the last term in (3) is a summation over all relaxation processes in the fluid. For clean fresh water, $\psi_{\nu} \equiv 0$, and (3) reduces to the standard KZK equation [21].

3.2 Axisymmetric Circular Source

When the source condition in the $z = 0$ plane corresponds to an axisymmetric, circular region such as a piston transducer or annular array, then (3) can be written as

$$\frac{\partial^2 p}{\partial t' \partial z} = \frac{c_0}{2} \left(\frac{\partial^2}{\partial r^2} + \frac{1}{r} \frac{\partial}{\partial r} \right) p + \frac{\delta}{2c_0^3} \frac{\partial^3 p}{\partial t'^3} + \frac{\beta}{2\rho_0 c_0^3} \frac{\partial^2 p^2}{\partial t'^2}$$

$$+ \sum_{\nu} \frac{m_{\nu}}{2c_0} \left(\frac{t_{\nu}}{1 + t_{\nu} \frac{\partial}{\partial t'}} \right) \frac{\partial^3 p}{\partial t'^3}, \quad (5)$$

where r is the radial coordinate. There are no known analytic solutions to (5), so it must be solved numerically. It is convenient to reduce this equation to a dimensionless form. Introduce the following scaling transformations:

$$P' = p/p_0, \quad \tau' = \omega_0 t', \quad R' = r/a, \quad (6)$$

$$\frac{\partial}{\partial t'} \rightarrow \omega_0 \frac{\partial}{\partial \tau'}, \quad (7)$$

$$\frac{\partial^2}{\partial r'^2} + \frac{1}{r} \frac{\partial}{\partial r} \rightarrow \frac{1}{a^2} \left(\frac{\partial^2}{\partial R'^2} + \frac{1}{R'} \frac{\partial}{\partial R'} \right), \quad (8)$$

where ω_0 is a characteristic angular frequency of the source waveform, and a is the radius of the circular source. These transformations lead to

$$\begin{aligned} \frac{\partial^2 P'}{\partial \tau' \partial z} &= \frac{1}{4z_r} \left(\frac{\partial^2}{\partial R'^2} + \frac{1}{R'} \frac{\partial}{\partial R'} \right) P' + \alpha_0 \frac{\partial^3 P'}{\partial \tau'^3} + \frac{1}{2z_s} \frac{\partial^2 P'^2}{\partial \tau'^2} \\ &+ \sum_{\nu} \frac{m_{\nu} \omega_0}{2c_0} \left(\frac{\tau_{\nu}}{1 + \tau_{\nu} \frac{\partial}{\partial \tau'}} \right) \frac{\partial^3 P'}{\partial \tau'^3}. \end{aligned} \quad (9)$$

Equation (9) introduces three new constants that characterize an axisymmetric circular source and the nonlinear wave propagation. The first, $z_r = \omega_0 a^2 / 2c_0$, is the well-known Rayleigh distance for a circular aperture. This distance is approximately the axial location where a linear acoustic field transitions from the so-called nearfield to the farfield. The second, $\alpha_0 = \delta \omega_0^2 / 2c_0^3$, is the thermoviscous attenuation coefficient. For an inhomogeneous plane wave and linear acoustics, α_0 is the distance the plane wave must travel for it to attenuate to e^{-1} of its original amplitude. The third constant, $z_s = \rho_0 c_0^3 / \beta \omega_0 p_0$, is the plane-wave shock formation distance. This is the distance an initially sinusoidal disturbance must propagate in order for the cumulative effects of the quadratic nonlinearity to produce shock formation. In addition, the dimensionless relaxation time is $\tau_{\nu} = \omega_0 t_{\nu}$.

All quantities in (9) have been scaled by an appropriate value except the z coordinate. Previous researchers have used either the Rayleigh distance for a flat piston source or the focal length of a weakly focused source for this scaling. A third possible choice for the length scale is the shock formation distance. To accommodate each of these choices, an arbitrary length scale l will be introduced such that

$$\sigma' = \frac{z}{l}, \quad \frac{\partial}{\partial z} \rightarrow \frac{1}{l} \frac{\partial}{\partial \sigma'}, \quad (10)$$

and (9) becomes

$$\frac{\partial^2 P'}{\partial \tau' \partial \sigma'} = \frac{l}{4z_r} \left(\frac{\partial^2}{\partial R'^2} + \frac{1}{R'} \frac{\partial}{\partial R'} \right) P' + \alpha_0 l \frac{\partial^3 P'}{\partial \tau'^3} + \frac{l}{2z_s} \frac{\partial^2 P'^2}{\partial \tau'^2}$$

$$+ \sum_{\nu} \frac{m_{\nu} \omega_0 l}{2c_0} \left(\frac{\tau_{\nu}}{1 + \tau_{\nu} \frac{\partial}{\partial \tau'}} \right) \frac{\partial^3 P'}{\partial \tau'^3}. \quad (11)$$

For a given pulse excitation in the $\sigma' = 0$ plane as a function of τ' and R' , (11) can be solved numerically by finite-difference and operator-splitting methods (see below).

Previous researchers have found that an additional coordinate transformation is useful, especially when diffraction becomes important. This change of coordinates is sometimes referred to as a “stretched coordinate” transformation because a rectangular grid in the transformed coordinate space (σ, R) corresponds to a grid that has been stretched in the original coordinate space (σ', R') . A complete discussion of this transformation is given by Lee [22]. A convenient form for the “stretched coordinate” transformation is

$$\sigma = \sigma', \quad P = (1 + \xi \sigma') P', \quad R = \frac{R'}{1 + \xi \sigma'}, \quad \tau = \tau' - \frac{\xi R'^2}{1 + \xi \sigma'}, \quad (12)$$

where the significance of the parameter ξ is discussed below. The differential operators in (11) become

$$\frac{\partial}{\partial \tau'} \rightarrow \frac{\partial}{\partial \tau}, \quad (13)$$

$$\frac{\partial}{\partial \sigma'} \rightarrow \frac{\partial}{\partial \sigma} - \frac{\xi R}{1 + \xi \sigma} \frac{\partial}{\partial R} + \xi^2 R^2 \frac{\partial}{\partial \tau}, \quad (14)$$

$$\begin{aligned} \frac{\partial^2}{\partial R'^2} + \frac{1}{R'} \frac{\partial}{\partial R'} &\rightarrow \frac{1}{(1 + \xi \sigma)^2} \left(\frac{\partial^2}{\partial R^2} + \frac{1}{R} \frac{\partial}{\partial R} \right) - \frac{4\xi}{1 + \xi \sigma} \frac{\partial}{\partial \tau} \\ &- \frac{4\xi R}{1 + \xi \sigma} \frac{\partial^2}{\partial R \partial \tau} + 4\xi^2 R^2 \frac{\partial^2}{\partial \tau^2}. \end{aligned} \quad (15)$$

Substitution of (12) to (15) into (11), integration with respect to τ' , and some tedious algebraic manipulations give

$$\begin{aligned} \frac{\partial P}{\partial \sigma} &= \frac{l}{4z_r(1 + \xi \sigma)^2} \int_{-\infty}^{\tau} \left(\frac{\partial^2}{\partial R^2} + \frac{1}{R} \frac{\partial}{\partial R} \right) P d\tau' + \alpha_0 l \frac{\partial^2 P}{\partial \tau^2} \\ &+ \frac{l}{z_s(1 + \xi \sigma)} P \frac{\partial P}{\partial \tau} + \sum_{\nu} \frac{m_{\nu} \omega_0 l}{2c_0} \left(\frac{\tau_{\nu}}{1 + \tau_{\nu} \frac{\partial}{\partial \tau}} \right) \frac{\partial^2 P}{\partial \tau^2} \\ &+ \frac{\xi}{1 + \xi \sigma} \left(1 - \frac{l}{z_r} \right) \frac{\partial(RP)}{\partial R} - \xi^2 R^2 \left(1 - \frac{l}{z_r} \right) \frac{\partial P}{\partial \tau}. \end{aligned} \quad (16)$$

If $\xi = 0$, then (16) reduces to essentially an identity transformation where the primes in (11) are dropped. When diffraction effects are expected to be minimal, as with a weakly focused source, then (11) can be used directly and l is the focal length. If $\xi = i$ and $l = z_r$, the transformation leads to the “stretched coordinate” system. Equation (16) is appropriate when diffraction is expected to be important. Finally, the last two terms in (16) can be ignored under these conditions on ξ and l .

3.3 Rectangular Source

When the source is rectangular with dimensions x_0 and y_0 , (3) can be written in the following dimensionless form:

$$\begin{aligned}\frac{\partial P}{\partial \sigma} = & \frac{l}{4x_r} \int_{-\infty}^{\tau} \frac{\partial^2 P}{\partial X^2} d\tau' + \frac{l}{4y_r} \int_{-\infty}^{\tau} \frac{\partial^2 P}{\partial Y^2} d\tau' + \alpha_0 l \frac{\partial^2 P}{\partial \tau^2} + \frac{l}{z_s} P \frac{\partial P}{\partial \tau} \\ & + \sum_{\nu} \frac{m_{\nu} \omega_0 l}{2c_0} \left(\frac{\tau_{\nu}}{1 + \tau_{\nu} \frac{\partial}{\partial \tau}} \right) \frac{\partial^2 P}{\partial \tau^2}.\end{aligned}\quad (17)$$

The distances $x_r = \omega_0 x_0^2 / 2c_0$ and $y_r = \omega_0 y_0^2 / 2c_0$ are defined in a manner consistent with the definition of the Rayleigh distance z_r , and X and Y are dimensionless Cartesian coordinates. Although the terms accounting for thermoviscous absorption, quadratic nonlinearity, and relaxation processes in (17) are similar to those terms in (16), these terms have implicit dependence on the Cartesian coordinates through $P(X, Y, \sigma, \tau)$. A transformation to a “stretch coordinate system” could be performed, but it has not been pursued. Baker et al. describe a transformed beam equation for a rectangular aperture that is based on a standard KZK equation [23]. Their result is essentially the “stretched coordinate” transform of (17) without relaxation.

4. NUMERICAL SOLUTION

There are no known analytic solutions to (3). Thus numerical solutions are the only available means to investigate nonlinear wave propagation from a bounded beam source. For a given pulse source condition $F(R, \sigma = 0, \tau)$, the axisymmetric source in Section 3.2 is a two-dimensional problem in (R, τ) of forward marching from σ to $\sigma + \Delta\sigma$. If $\Delta\sigma$ is small, then (16) can be solved via an operator-splitting method [24]. That is, the following system of equations is equivalent to (16):

$$\frac{\partial P}{\partial \sigma} = \frac{1}{4G(1 + \xi\sigma)^2} \int_{-\infty}^{\tau} \left(\frac{\partial^2}{\partial R^2} + \frac{1}{R} \frac{\partial}{\partial R} \right) P d\tau', \quad (18)$$

$$\frac{\partial P}{\partial \sigma} = A \frac{\partial^2 P}{\partial \tau^2}, \quad (19)$$

$$\frac{\partial P}{\partial \sigma} = \frac{NP}{1 + \xi\sigma} \frac{\partial P}{\partial \tau}, \quad (20)$$

$$\left(1 + \tau_{\nu} \frac{\partial}{\partial \tau} \right) \frac{\partial P}{\partial \sigma} = C_{\nu} \frac{\partial^2 P}{\partial \tau^2} \quad (21)$$

(subject to the above conditions on ξ and l). In these equations, $G = z_r/l$ is known as the focusing gain, $A = \alpha_0 l$ is a thermoviscous absorption constant, $N = l/z_s$ is a nonlinearity constant, and $C_{\nu} = m_{\nu} \tau_{\nu} \omega_0 l / 2c_0$ is a dimensionless parameter. Equation (21) is applied to each relaxation process.

Numerical integration of (18)–(21) requires the specification of a discrete, finite domain in (R, τ) and appropriate conditions at the edge of this domain. The finite domain is $R \in [0, R_M]$ and $\tau \in [\tau_m, \tau_M]$; R_M is chosen large enough to eliminate a possible reflection from the nonabsorbing boundary. The minimum and maximum dimensionless retarded time, τ_m and τ_M , are chosen such that a zero-amplitude period of time precedes and follows the finite pulse, permitting the pulse to propagate without edge effects from the finite domain. Furthermore, the following conditions are imposed:

$$P(\sigma, R, \tau_m) = 0, \quad P(\sigma, R, \tau_M) = 0, \quad P(\sigma, R_M, \tau) = 0, \quad \left. \frac{\partial P}{\partial R} \right|_{R=0} = 0. \quad (22)$$

The last condition is essentially a symmetry condition along the axis of the circular source. Introduction of the fixed increments $\Delta\tau$ and ΔR allows a discrete grid to be defined such that $\tau \in [\tau_m, \tau_M] \iff i \in [0, I]$ and $R \in [0, R_M] \iff j \in [0, J]$, where $P(\sigma, R, \tau) \equiv P(\sigma_k, j\Delta R, \tau_m + i\Delta\tau) = P_{i,j}^k$ and the first three conditions in (22) reduce to $P_{0,j}^k = 0$, $P_{I,j}^k = 0$, and $P_{i,0}^k = 0$.

Standard finite-difference (FD) techniques can be implemented to solve (18), (19), and (21). The integration in (18) is first approximated with a standard trapezoid

quadrature. The details of reducing these equations to FD algorithms are given by Lee [22] and therefore are omitted from the present report. Under source conditions of interest to Lee, it was observed that implicit backward FD algorithms were required near the source plane. At a sufficient distance from this plane, the numerical integrations could be switched to Crank-Nicolson algorithms. The numerical advantages of the Crank-Nicolson scheme with respect to an implicit backward method are discussed at length in standard texts on FD techniques [25]. Finally, analyses of the truncation errors show that the following algorithms are accurate in $\Delta\sigma$, ΔR , and $\Delta\tau$ to at least first order.

The equation governing nonlinear steepening, (20), yields an analytic solution. If the dimensionless pressure is $P(\sigma, R, \tau)$, then it can be shown by direct substitution that

$$P(\sigma + \Delta\sigma, R, \tau) = P(\sigma, R, \tau + NP\phi_\sigma) \quad (23)$$

is a solution to (20). The factor ϕ_σ in our notation is

$$\phi_\sigma = \begin{cases} \frac{1}{\xi} \ln \left(1 + \frac{\xi \Delta\sigma}{1 + \xi\sigma} \right), & \xi > 0, \\ \Delta\sigma, & \xi = 0. \end{cases} \quad (24)$$

Again, the details are given by Lee [22]. The numerical algorithm is described below. Furthermore, a single algorithm suffices through the entire σ domain.

4.1 Diffraction Algorithm

The diffraction integral, the symmetry condition along the axis of the source, and the nonabsorbing boundary condition at $R = R_M$ suggest that the FD algorithm should give explicit expressions for $j = 0, 1 \leq j < J-1$, and $j = J-1$ for $i \in [1, I-1]$. The implicit backward FD (IBFD) algorithm is

$$(1 - D_2)P_{i,0}^{k+1} + D_2P_{i,1}^{k+1} = P_{i,0}^k - D_1(S_1 - S_0), \quad (25)$$

$$D_8f_j^-P_{i,j-1}^{k+1} + (1 - D_4)P_{i,j}^{k+1} + D_8f_j^+P_{i,j+1}^{k+1} = P_{i,j}^k + D_2S_j - D_4(f_j^+S_{j+1} + f_j^-S_{j-1}), \quad (26)$$

$$D_8f_{J-1}^-P_{i,J-2}^{k+1} + (1 - D_4)P_{i,J-1}^{k+1} = P_{i,J-1}^k - D_4f_{J-1}^-S_{J-2} + D_2S_{J-1}, \quad (27)$$

where

$$D_n = -\frac{\Delta\tau\Delta_k\sigma}{nG(\Delta R)^2(1 + \xi\sigma_{k+1})^2}, \quad f_j^\pm = 1 \pm \frac{1}{2j}, \quad S_j = \sum_{m=1}^{i-1} P_{m,j}^{k+1}. \quad (28)$$

The first equation of (28) is a constant for a given $\Delta_k\sigma$ step. The subscript k on Δ indicates that an adaptive step-size is possible in σ . In fact, in the vicinity of a strong, rapid, change in pressure, $\Delta\sigma$ needs to be *small* to prevent the occurrence of an unphysical multivalued waveform during the nonlinear step described by (20). The second and third equations in (28) arise from the diffraction integral in (18) and its subsequent approximation by trapezoid quadrature. (Note: The values $P_{m,j}^k$ in the summation occur at previous moments in time.) The Crank-Nicolson FD (CNFD) algorithm is

$$\frac{1}{2}(1 - D_4)Q_{i,0}^{k+1} + D_8Q_{i,1}^{k+1} = P_{i,0}^k - D_4(S'_1 - S'_0), \quad (29)$$

$$D_{32}f_j^-Q_{i,j-1}^{k+1} + \frac{1}{2}(1 - D_8)Q_{i,j}^{k+1} + D_{32}f_j^+Q_{i,j+1}^{k+1} = P_{i,j}^k + D_8S'_j - D_{16}(f_j^+S'_{j+1} + f_j^-S'_{j-1}), \quad (30)$$

$$D_{32}f_{j-1}^-Q_{i,j-2}^{k+1} + \frac{1}{2}(1 - D_8)Q_{i,j-1}^{k+1} = P_{i,j-1}^k - D_{16}f_{j-1}^-S'_{j-2} + D_8S'_{j-1}, \quad (31)$$

where

$$Q_{i,j}^{k+1} = P_{i,j}^{k+1} + P_{i,j}^k, \quad S'_j = \sum_{m=1}^{i-1} Q_{m,j}^{k+1}. \quad (32)$$

Inspection of (25)–(27) and (29)–(31) shows that the IBFD and CNFD algorithms form tridiagonal systems of equations. A standard matrix method, known as the Thomas algorithm, permits a rapid solution to these equations.

4.2 Thermoviscous Absorption Algorithm

The IBFD algorithm for the equation governing thermoviscous absorption can be written as

$$A'P_{i-1,j}^{k+1} + (1 - 2A')P_{i,j}^{k+1} + A'P_{i+1,j}^{k+1} = P_{i,j}^k, \quad (33)$$

where $A' = -A\Delta_k\sigma/(\Delta\tau)^2$. The corresponding CNFD algorithm is

$$\frac{A'}{2}P_{i-1,j}^{k+1} + (1 - A')P_{i,j}^{k+1} + \frac{A'}{2}P_{i+1,j}^{k+1} = (1 + A')P_{i,j}^k - \frac{A'}{2}(P_{i-1,j}^k + P_{i+1,j}^k). \quad (34)$$

When edge conditions $P_{0,j}^k$ and $P_{I,j}^k$ are introduced into (33) and (34), it is seen that tridiagonal systems of equations are recovered.

4.3 Quadratic Nonlinearity Algorithm

As stated previously, the quadratic nonlinearity manifests an analytic solution. The numerical implementation of (23) and (24) involves two steps. First, the waveform for each radial value j is distorted onto a nonuniform $\tilde{\tau}$ grid. This is accomplished by

$$\tilde{\tau}_{i,j}^k = \tau_{i,j}^k - NP_{i,j}^k \phi_{\sigma_k}. \quad (35)$$

Here, $\tau_{i,j}^k$ are the uniformly spaced dimensionless retarded time points such that $\Delta\tau = \tau_{i,j}^k - \tau_{i-1,j}^k$, and $\tilde{\tau}_{i,j}^k$ are the new retarded time points which are not uniformly spaced. Both $P_{i,j}^k$ and ϕ_{σ_k} are evaluated at the current σ_k location. As can be seen in Figure 10, this phase distortion “slides” the pressure amplitude values to new retarded times.

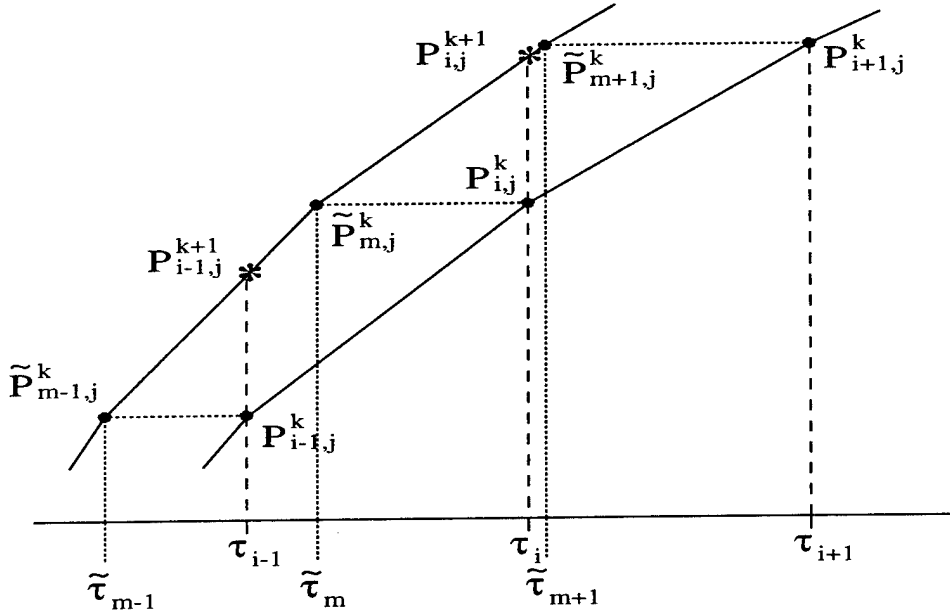


Figure 10. The curve on the right is the discrete pressure at σ_k and the curve on the left results from applying the nonlinear algorithm. The asterisk on the left curve is the final value of pressure, $P_{i,j}^{k+1}$, after the resampling step.

The second step entails a resampling of the distorted waveform back onto the uniform retarded time grid. This step is necessary because the finite-difference algorithms for diffraction, thermoviscous absorption, and relaxation assume a uniform grid. Simple linear interpolation is used to resample the waveform;

$$P_{i,j}^{k+1} = \left(\frac{\tilde{P}_{m+1,j}^k - \tilde{P}_{m,j}^k}{\tilde{\tau}_{m+1,j}^k - \tilde{\tau}_{m,j}^k} \right) (\tau_{i,j}^k - \tilde{\tau}_{m,j}^k) + \tilde{P}_{m,j}^k, \quad (36)$$

where $\tilde{P}_{m,j}^k$ is the pressure amplitude corresponding to $\tilde{\tau}_{m,j}^k$. A pictorial description of these steps is contained in Figure 10.

Physically, a valid solution of (23) is constrained to be a single-valued function of retarded time. The algorithm here does not guarantee this requirement, and hence application of (35) means that a strict ordering of $\tilde{\tau}_{m,j}^k \leq \tilde{\tau}_{m+1,j}^k$ must be maintained. The desired ordering can be imposed by selecting $\Delta_k \sigma$ to be an appropriately small value; in fact, an adaptive step-size in σ can be implemented by requiring

$$\Delta_k \sigma \leq \left(2N \left. \frac{\partial \tilde{P}}{\partial \tilde{\tau}} \right|_{\max} \right)^{-1}, \quad (37)$$

where the subscript “max” denotes the maximum slope in the newly distorted waveform.

As a final note, the nonlinear steepening of a waveform shifts energy from lower-frequency components to higher frequencies. The algorithm in (35) is essentially exact (to within numerical round-off errors) and is certainly more accurate than the finite-difference algorithms. However, the resampling step produces an artificial smoothing of the waveform because $\Delta\tau$ is always larger than some step sizes on the nonuniform $\tilde{\tau}_{m,j}^k$ grid. The smoothing acts as a low-pass filter. Hence for accurate numerical simulations $\Delta\tau$ must be chosen to accommodate the highest frequency of interest.

4.4 Relaxation Algorithm

The IBFD algorithm for the ν th relaxation process is

$$-\lambda_\nu^+ P_{i-1,j}^{k+1} + (1 + 2C'_\nu) P_{i,j}^{k+1} - \lambda_\nu^- P_{i+1,j}^{k+1} = P_{i,j}^k + \tau'_\nu (P_{i+1,j}^k - P_{i-1,j}^k), \quad (38)$$

where $C'_\nu = C_\nu(\Delta\sigma)_k / (\Delta\tau)^2$, $\tau'_\nu = \tau_\nu / 2\Delta\tau$, and $\lambda_\nu^\pm = C'_\nu \pm \tau'_\nu$. The Crank-Nicolson method yields

$$-\Lambda_\nu^+ P_{i-1,j}^{k+1} + 2(1 + C'_\nu) P_{i,j}^{k+1} - \Lambda_\nu^- P_{i+1,j}^{k+1} = 2(1 - C'_\nu) P_{i,j}^k + \Lambda_\nu^- P_{i-1,j}^k + \Lambda_\nu^+ P_{i+1,j}^k, \quad (39)$$

such that $\Lambda_\nu^\pm = \lambda_\nu^\pm \pm \tau'_\nu$.

APPENDIX

Empirical Material Parameters for Water

In Section 3, several symbols are introduced to represent physical properties of the fluid. Standard handbooks provide limited tables for these properties for water; however many are restricted to small ranges of temperature, ambient pressure, and salinity [26]. One is forced to scour the literature to obtain a complete set of parameter for any given computation. The purpose of this appendix is to compile several empirical relationships for these parameters. An empirical rule for the parameter of nonlinearity, B/A , for water is not available, so a table of values from the literature is provided. The table permits linear interpolation for values not contained explicitly in the table.

The small-signal sound speed, c_0 , can be approximated from the Chen-Millero-Li equation [27], which is an empirical fit to a large range of data. It has explicit dependence on temperature, ambient pressure relative to 1 atm, and salinity. These quantities are denoted respectively by T , P , and S . The Chen-Millero-Li equation is

$$c_0 = c_w(P, T) - c_c(P, T) + a(P, T)S + b(P, T)S^{3/2} + d(P)S^2, \quad (40)$$

where the auxiliary functions are

$$\begin{aligned} c_w(P, T) = & 1402.388 + 5.03711T - 0.0580852T^2 + 3.3420 \times 10^{-4}T^3 \\ & - 1.4780 \times 10^{-6}T^4 + 3.1464 \times 10^{-9}T^5 + (0.153563 + 6.8982 \times 10^{-4}T \\ & - 8.1788 \times 10^{-6}T^2 + 1.3621 \times 10^{-7}T^3 - 6.1185 \times 10^{-10}T^4)P \\ & + (3.1260 \times 10^{-5} - 1.7107 \times 10^{-6}T + 2.5974 \times 10^{-8}T^2 - 2.5335 \times 10^{-10}T^3 \\ & + 1.0405 \times 10^{-12}T^4)P^2 - (9.7729 \times 10^{-9} - 3.8504 \times 10^{-10}T \\ & + 2.3643 \times 10^{-12}T^2)P^3, \end{aligned} \quad (41)$$

$$\begin{aligned} c_c(P, T) = & (0.0029 - 2.19 \times 10^{-4}T + 1.4 \times 10^{-5}T^2)P - (4.76 \times 10^{-6} \\ & - 3.47 \times 10^{-7}T + 2.59 \times 10^{-8}T^2)P^2 + 2.68 \times 10^{-9}P^3, \end{aligned} \quad (42)$$

$$\begin{aligned} a(P, T) = & 1.389 - 0.01262T + 7.164 \times 10^{-5}T^2 + 2.006 \times 10^{-6}T^3 - 3.21 \times 10^{-8}T^4 \\ & + (9.4742 \times 10^{-5} - 1.2580 \times 10^{-5}T - 6.4885 \times 10^{-8}T^2 + 1.0507 \times 10^{-8}T^3 \\ & - 2.0122 \times 10^{-10}T^4)P - (3.9064 \times 10^{-7} - 9.1041 \times 10^{-9}T \\ & + 1.6002 \times 10^{-10}T^2 - 7.988 \times 10^{-12}T^3)P^2 + (1.100 \times 10^{-10} \\ & + 6.649 \times 10^{-12}T - 3.389 \times 10^{-13}T^2)P^3, \end{aligned} \quad (43)$$

$$b(P, T) = -0.01922 - 4.42 \times 10^{-5}T + (7.3637 \times 10^{-5} + 1.7945 \times 10^{-7}T)P, \quad (44)$$

$$d(P) = 0.001727 - 7.9836 \times 10^{-6}P. \quad (45)$$

Equations (40) to (45) are subject to the following restrictions: $0 \leq T \leq 40^\circ\text{C}$, $0 \leq S \leq 40$ ppt, and $0 \leq P \leq 1000$ bar. Within the applicable ranges on T , P , and

S , the Chen-Millero-Li formula is claimed to be accurate to ± 0.05 m/s, where c_0 has units of meters per second. Finally, it is restated that P has units of bar.

The density of the ambient fluid, specific heat at constant pressure, specific heat at constant volume, and the thermal conductivity are determined by the following empirical equations [28]:

$$\rho_0 = \begin{cases} 999.7 + 0.048 \times 10^{-5}P - 0.088\Delta T - 0.007(\Delta T)^2, \\ 1027 + 0.043 \times 10^{-5}P - 0.16\Delta T - 0.004(\Delta T)^2 + 0.75\Delta S, \end{cases} \quad (46)$$

$$c_p = \begin{cases} 4192 - 0.40 \times 10^{-5}P - 1.6\Delta T, \\ 3988 - 0.23 \times 10^{-5}P + 0.54\Delta T - 5.4\Delta S, \end{cases} \quad (47)$$

$$c_v = \begin{cases} c_p[1 - 0.0011(1 + \Delta T/6 + 0.0024 \times 10^{-5}P)^2], \\ c_p[1 - 0.0041(1 + \Delta T/20 + 0.0012 \times 10^{-5}P + 0.012\Delta S)^2], \end{cases} \quad (48)$$

$$\kappa = 0.597 + 0.0017\Delta T - 7.5 \times 10^{-6}(\Delta T)^2. \quad (49)$$

The upper expressions for ρ_0 , c_p , and c_v apply to fresh water, and the lower expressions apply to sea water. The salinity is taken relative to 35 ppt (i.e., $\Delta S = S - 35$), and the relative temperature is $\Delta T = T - 273.16$ K. Unlike the Chen-Millero-Li equation, P is absolute pressure in units of pascal and T is specified in kelvin. The units are kilograms per cubic meter for ρ_0 , joules per kilogram per kelvin for c_p and c_v , and watts per meter per kelvin for κ . Finally, Pierce states that the thermal conductivity is essentially constant with respect to changes in salinity and pressure. Hence, (49) is sufficient for both fresh and sea water, and it should deviate by no more than a few percent from the actual value for κ .

The shear viscosity of water appears to be insensitive to changes in salinity and ambient pressure but varies with temperature. A standard handbook [26] containing physical properties for water gives the following empirical formulae:

$$\log \eta = \begin{cases} \frac{1301}{998.333 + 8.1855\Delta T + 0.00585(\Delta T)^2} - 3.30233, & 0 \leq T \leq 20, \\ -\frac{1.3272\Delta T + 0.001053(\Delta T)^2}{\Delta T + 125} + 8.6772 \times 10^{-3}, & 20 < T \leq 100, \end{cases} \quad (50)$$

where temperature is given in celsius such that $\Delta T = T - 20$. The bulk viscosity of a fluid is often ignored because of assumptions of irrotational flow and incompressible fluid dynamics. Pierce states that ζ is relatively constant for changes in P and S and it has a weak dependence on temperature. Bulk viscosity for water can be approximated by

$$\zeta/\eta = -0.29T/60.0 + 3.01, \quad (51)$$

where the temperature range is $0 \leq T \leq 60^\circ\text{C}$. The units for η and ζ are centipoise.

The parameter of nonlinearity, B/A , is related to the coefficient of nonlinearity by $\beta = 1 + B/2A$ for a fluid. Limited data inhibit an accurate empirical formula to estimate B/A for either fresh water or sea water [29, 30]. Estimates of B/A are obtained via linear interpolation from the values listed in Table 1. Pierce states that nearly 99.5% of sea water falls into a salinity range from 33 to 37 ppt. Hence, estimating B/A from this table is adequate for the numerical computations.

Table 1. B/A values for fresh and sea water.

T (°C)	0	10	20	30	40	60	80	100
$S = 0$	4.2		5.0		5.4	5.7	6.1	6.1
$S = 33$	4.9	5.1	5.2	5.4				
$S = 35$				5.25				

The empirical models for sea water are completed once formulae for the dimensionless relaxation time, $\tau_\nu = \omega_0 t_\nu$, and dimensionless dispersion parameter, $C_\nu = m_\nu \tau_\nu \omega_0 l / 2c_0$, are determined for the various relaxation processes. As stated in Section 1, the presence of H_3BO_3 and MgSO_4 in sea water provides the dominate energy loss through relaxation mechanisms. Francois and Garrison give the following empirical formula for the attenuation coefficients:

$$\alpha_\nu = \frac{A_\nu P_\nu f_\nu f^2}{f^2 + f_\nu^2} \quad (52)$$

where f_ν is the relaxation frequency and A_ν and P_ν are coefficients that depend on P , S , and T as well as the pH for H_3BO_3 [1, 2]. Hence t_ν and m_ν can be related to α_ν via consideration of (21) and an inhomogeneous plane-wave $\exp(ikz - i\omega t)$, where $\alpha_\nu = \Im(k)$. Simple algebraic manipulations lead to

$$t_\nu = 1/2\pi f_\nu, \quad m_\nu = A_\nu P_\nu c_0 / \pi \quad (53)$$

and

$$\tau_\nu = \omega / 2\pi f_\nu, \quad C_\nu = (1 + \tau_\nu^2) \alpha_\nu l. \quad (54)$$

The units of f_ν and A_ν are, respectively, hertz and nepers per meter per hertz while P_ν is unitless. For H_3BO_3 , the parameters are

$$f_1 = 2800(S/35)^{1/2} 10^{(4-1245/\theta)}, \quad (55)$$

$$A_1 = 1.0200 \times 10^{(0.78pH-11)}/c, \quad (56)$$

$$P_1 = 1, \quad (57)$$

$$c = 1412 + 3.21T + 1.19S + 0.0167D, \quad (58)$$

where $\theta = T + 273$ and T , S , and D (depth) have units of celsius, parts per thousand, and meters, respectively. For MgSO_4 , these parameters are identified as

$$f_2 = [8.17 \times 10^{(11-1990/\theta)}] / [1 + 0.0018(S - 35)], \quad (59)$$

$$A_2 = 2.4683 \times 10^{-6} S (1 + 0.0025T) / c, \quad (60)$$

$$P_2 = 1 - (1.37 \times 10^{-4} - 6.2 \times 10^{-9} D) D, \quad (61)$$

where c in (60) is given by (58).

REFERENCES

- [1] R. E. Francois and G. R. Garrison, "Sound absorption based on ocean measurements: Part I: Pure water and magnesium sulfate contributions," *J. Acoust. Soc. Am.*, **72**, 896–907 (1982).
- [2] R. E. Francois and G. R. Garrison, "Sound absorption based on ocean measurements: Part II: Boric acid contribution and equation for total absorption," *J. Acoust. Soc. Am.*, **72**, 1879–1890 (1982).
- [3] K. W. Commander and A. Prosperetti, "Linear pressure waves in bubbly liquids: Comparison between theory and experiment," *J. Acoust. Soc. Am.*, **85**, 732–746 (1989).
- [4] K. Commander and E. Moritz, "Off-resonance contributions to acoustical bubble spectra," *J. Acoust. Soc. Am.*, **85**, 2665–2669 (1989).
- [5] I. N. Kozhevnikova and L. Bjørnø, "Nonlinear effects by bubble cloud oscillations near the sea surface," in "Frontiers of Nonlinear Acoustics: Proceedings of 12th ISNA," edited by M. F. Hamilton and D. T. Blackstock (Elsevier, London) (1990), pp. 509–513.
- [6] L. M. Lyamshev and P. V. Sakov, "Nonlinear interaction of a plane wave and a spherical wave," *Sov. Phys. Acoust.*, **34**, 281–284 (1988).
- [7] P. V. Sakov, "Nonlinear interaction of nonconcentric spherical waves," *Sov. Phys. Acoust.*, **38**, 180–183 (1992).
- [8] P. V. Sakov, "Nonlinear interaction of nonconcentric spherical waves in an ideal fluid," *Physics-Doklady*, **40**, 166–169 (1995).
- [9] J. H. Ginsberg and M. F. Hamilton, "Computational Methods," in "Nonlinear Acoustics," edited by M. F. Hamilton and D. T. Blackstock (Academic, San Diego), chap. 11, pp. 309–341 (1997).
- [10] Y.-S. Lee and M. F. Hamilton, "Time-domain modeling of pulsed fine-amplitude sound beams," *J. Acoust. Soc. Am.*, **97**, 906–917 (1995).
- [11] E. E. McDonald and W. A. Kuperman, "Time domain formulation for pulse propagation including nonlinear behavior at a caustic," *J. Acoust. Soc. Am.*, **81**, 1406–1417 (1987).
- [12] B. E. McDonald, P. Caine, and M. West, "A tutorial on the nonlinear progressive wave equation (NPE) – Part 1," *Appl. Acoust.*, **43**, 159–167 (1994).

- [13] R. O. Cleveland, M. F. Hamilton, and D. T. Blackstock, "Time-domain modeling of finite-amplitude sound in relaxing fluids," *J. Acoust. Soc. Am.*, **99**, 3312–3318 (1996).
- [14] J. A. Shooter, T. G. Muir, and D. T. Blackstock, "Acoustic saturation of spherical waves in water," *J. Acoust. Soc. Am.*, **55**, 54–62 (1974).
- [15] D. H. Trivett and A. L. Van Buren, "Propagation of plane, cylindrical, and spherical finite amplitude waves," *J. Acoust. Soc. Am.*, **69**, 943–949 (1981).
- [16] P. Edson and R. A. Roy, "Nonlinear wave propagation from a discrete annular array," Tech. Rep. AM-98-038, Dept. of Aerospace and Mech. Eng., Boston University (1998).
- [17] M. A. Averkiou and M. F. Hamilton, "Nonlinear distortion of short pulses radiated by plane and focused circular pistons," *J. Acoust. Soc. Am.*, **102**, 2539–2548 (1997).
- [18] D. A. Hutchins, H. D. Mair, and R. G. Taylor, "Transient pressure fields of PVDF transducers," *J. Acoust. Soc. Am.*, **82**, 183–192 (1987).
- [19] J. N. Tjøtta and S. Tjøtta, "Nonlinear Equations of Acoustics," in "Frontiers of Nonlinear Acoustics: Proceedings of 12th ISNA," edited by M. F. Hamilton and D. T. Blackstock (Elsevier, London) (1990), pp. 80–97.
- [20] R. O. Cleveland, "Propagation of sonic booms through a real, stratified atmosphere," Ph.D. thesis, The University of Texas at Austin (1995).
- [21] M. F. Hamilton, "Sound Beams," in "Nonlinear Acoustics," edited by M. F. Hamilton and D. T. Blackstock (Academic, San Diego), chap. 8, pp. 233–261 (1997).
- [22] Y.-S. Lee, "Numerical solution of the kz_k equation for pulsed finite amplitude sound beams in thermoviscous fluids," Ph.D. thesis, The University of Texas at Austin (1993).
- [23] A. C. Baker, A. M. Berg, A. Sahin, and J. N. Tjøtta, "The nonlinear pressure field of plane, rectangular apertures: Experimental and theoretical results," *J. Acoust. Soc. Am.*, **97**, 3510–3517 (1995).
- [24] R. J. LeVeque, *Numerical Methods for Conservation Laws* (Birkhäuser, Boston) (1992).
- [25] J. C. Strikwerda, *Finite Difference Schemes and Partial Differential Equations* (Wadsworth, Belmont, CA) (1989).

- [26] R. C. Yeast and M. J. Astle, eds., *CRC Handbook of Chemistry and Physics* (CRC, Boca Raton, FL) (1980).
- [27] “APL-UW high-frequency ocean environmental acoustic models handbook,” Tech. Rep. APL-UW TR 9407, Applied Physics Laboratory, University of Washington, 1994.
- [28] A. D. Pierce, *Acoustics—An Introduction to Its Physical Principles and Applications* (Acoust. Soc. Am., Woodbury, New York) (1989).
- [29] R. T. Beyer, “Nonlinear Acoustics (Experimental),” in “American Institute of Physics Handbook,” edited by D. E. Gray (McGraw-Hill, New York), chap. 3, pp. 3–207–210 (1972).
- [30] R. T. Beyer, “The parameter B/A ,” in “Nonlinear Acoustics,” edited by M. F. Hamilton and D. T. Blackstock (Academic, San Diego), chap. 2, pp. 25–39 (1997).

REPORT DOCUMENTATION PAGE

Form Approved
OPM No. 0704-0188

Public reporting burden for this collection of information is estimated to average 1 hour per response, including the time for reviewing instructions, searching existing data sources, gathering and maintaining the data needed, and reviewing the collection of information. Send comments regarding this burden estimate or any other aspect of this collection of information, including suggestions for reducing this burden, to Washington Headquarters Services, Directorate for Information Operations and Reports, 1215 Jefferson Davis Highway, Suite 1204, Arlington, VA 22202-4302, and to the Office of Information and Regulatory Affairs, Office of Management and Budget, Washington, DC 20503.

1. AGENCY USE ONLY (Leave blank)	2. REPORT DATE	3. REPORT TYPE AND DATES COVERED	
	September 1998	Technical	
4. TITLE AND SUBTITLE Nonlinear Wave Propagation with Implications for Mine Neutralization			5. FUNDING NUMBERS Contract N00039-91-C-0072
6. AUTHOR(S) Steven G. Kargl			
7. PERFORMING ORGANIZATION NAME(S) AND ADDRESS(ES) Applied Physics Laboratory University of Washington 1013 NE 40th Street Seattle, WA 98105-6698			8. PERFORMING ORGANIZATION REPORT NUMBER APL-UW TR 9803
9. SPONSORING / MONITORING AGENCY NAME(S) AND ADDRESS(ES) Office of Naval Research Code 321 800 N. Quincy Street Arlington, VA 22217			10. SPONSORING / MONITORING AGENCY REPORT NUMBER
11. SUPPLEMENTARY NOTES			
12a. DISTRIBUTION / AVAILABILITY STATEMENT Approved for public release; distribution is unlimited.		12b. DISTRIBUTION CODE	
13. ABSTRACT (Maximum 200 words) Prototype devices that use pulse-power techniques to generate an intense acoustical field in water have fostered a renewed interest in applying finite-amplitude sound to the mine-neutralization problem, particularly in a littoral region. A simple intuitive description of acoustical mine neutralization includes three basic processes: (1) generation of the acoustical field at the source; (2) nonlinear wave propagation; and (3) neutralization mechanisms at the target. This document focuses on the second issue, the propagation of an intense acoustical field from a source to a target. The research discussed here provides a theoretical foundation for a modeling effort, describes several case studies, and gives empirical rules for establishing the material parameters of fresh and sea water required by the theory. Several key issues are presented, including the breakdown of using linear superposition of the results for discrete sources in an array, phasing an array of discrete sources for beam steering, and peak positive and negative pressures.			
14. SUBJECT TERMS Nonlinear acoustics, mine countermeasures, neutralization, phased array of intense sources			15. NUMBER OF PAGES 35
			16. PRICE CODE
17. SECURITY CLASSIFICATION OF REPORT Unclassified	18. SECURITY CLASSIFICATION OF THIS PAGE Unclassified	19. SECURITY CLASSIFICATION OF ABSTRACT Unclassified	20. LIMITATION OF ABSTRACT SAR